LETTERS

Visualizing dislocation nucleation by indenting colloidal crystals

Peter Schall[1]†, Itai Cohen[1,2]†, David A. Weitz[1,2] & Frans Spaepen[1]

The formation of dislocations is central to our understanding of yield, work hardening, fracture, and fatigue[1] of crystalline materials. While dislocations have been studied extensively in conventional materials, recent results have shown that colloidal crystals offer a potential model system for visualizing their structure and dynamics directly in real space[2]. Although thermal fluctuations are thought to play a critical role in the nucleation of these defects, it is difficult to observe them directly. Nano-indentation, during which a small tip deforms a crystalline film, is a common tool for introducing dislocations into a small volume that is initially defect-free[3–10]. Here, we show that an analogue of nano-indentation performed on a colloidal crystal provides direct images of defect formation in real time and on the single particle level, allowing us to probe the effects of thermal fluctuations. We implement a new method to determine the strain tensor of a distorted crystal lattice and we measure the critical dislocation loop size and the rate of dislocation nucleation directly. Using continuum models, we elucidate the relation between thermal fluctuations and the applied strain that governs defect nucleation. Moreover, we estimate that although bond energies between particles are about fifty times larger in atomic systems, the difference in attempt frequencies makes the effects of thermal fluctuations remarkably similar, so that our results are also relevant for atomic crystals.

To reduce strain energies, colloidal crystals nucleate dislocations, which mark the boundary of a surface along which the crystal has been uniformly sheared[1]. Dislocation nucleation reflects a competition between the energy cost for creating a dislocation loop and the energy gain from the strain relieved by the shear along the surface bounded by the loop. The nucleation energy reaches a maximum, U_c, at the critical loop radius, r_c. Therefore, dislocations are formed only if the loops become greater than r_c. The energy barrier for defect nucleation depends sensitively on the applied strain; at low strains, thermal fluctuations are the only means of overcoming this barrier. While recent *in situ* techniques allow the imaging of the evolution of dislocations on a medium-range length scale during indentation using transmission electron microscopy[9,10], the nucleation of dislocation loops and the consequences of thermal effects are extremely difficult to observe directly in atomic systems.

We grow a 43-μm-thick face-centred cubic (f.c.c.) crystal in the [100] direction by slowly sedimenting 1.55-μm-diameter silica particles onto a patterned [100] substrate[11]. The silica particles are suspended in a mixture of water and dimethylsulphoxide (DMSO), which matches their refractive index. We add a small amount of fluorescein to the solvent so that under fluorescence the particles appear as dark spots on a bright background. By varying the crystal thickness we confirm that in this crystal sufficient thermally induced particle motion persists that the effects of thermal fluctuations can still be observed on reasonable timescales. We indent the crystal with a sewing needle (Singer sewing needles, 25 assorted sharps) attached to a piezoelectric translation stage. The needle has an almost-hemispherical tip with a diameter of 40 μm; this tip shape induces a strain field whose maximum shear strain is well below the contact surface, and is commonly used for studying dislocation nucleation. The length scale ratios between tip diameter, particle radius, and film thickness are similar to the ratios used in nano-indentation experiments; thus the experiments are comparable.

We use laser diffraction microscopy (LDM)[2] to obtain an overview of the dislocation nucleation process. The incident beam forms a 36°

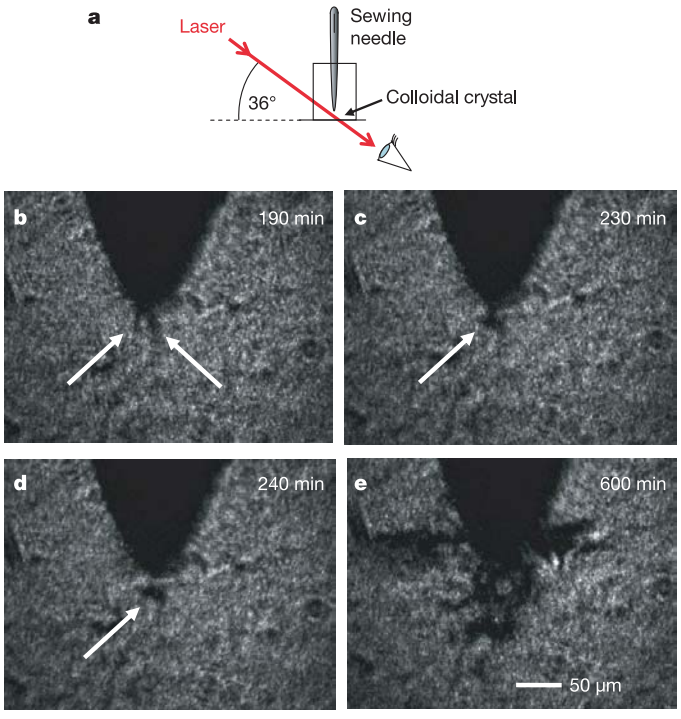

Figure 1 | Laser diffraction microscopy images of defect structure. **a**, Schematic of the indentation configuration. The imaging line of sight (red line) forms a 36° angle with the template and corresponds to the [111] direction of the f.c.c. lattice. **b**–**e**, LDM images depicting dark regions that correspond to crystal lattice distortions. **b**, Arrows indicate two dark regions observed at $t = 190$ min. These regions first appear at $t = 160$ min and persist until $t = 220$ min. **c**, **d**, Arrows indicate a dislocation loop that becomes detached from the needle. **e**, Final dislocation structure at $t = 600$ min.

[1]Division of Engineering and Applied Sciences, [2]Department of Physics, Harvard University, 9 Oxford Street, Cambridge, Massachusetts 02138, USA. †Present addresses: Van der Waals-Zeeman Institute, University of Amsterdam, Valckenierstraat 65, 1018 XE Amsterdam, The Netherlands (P.S.); Department of Physics, Cornell University, 508 Clark Hall, Ithaca, NY 14853, USA (I.C.).

angle with the plane of the template and is parallel to the [111] direction of the f.c.c. crystal (Fig. 1a). We use the transmitted beam for imaging the defect structure. LDM exploits the difference in scattering between the perfect and the distorted crystal lattices near the dislocation core, and produces a real-space image in which dislocations appear as dark lines on a bright background. We lower the needle at a rate of $3.4\,\mu m\,h^{-1}$ and record LDM images (see Supplementary Information video). Surprisingly, even before the needle touches the crystal, thermal effects produce local intensity fluctuations which last several seconds.

Four images of the indented crystal are shown in Fig. 1. About 190 min after we start lowering the needle, we observe two dark regions beneath the needle tip (arrows in Fig. 1b), which we associate with the strained lattice. Remarkably, these regions exhibit intensity fluctuations that last several minutes. This suggests that, in the strained lattice, thermal fluctuations become more spatially correlated, and persist over longer timescales than in the unstrained lattice. After 230 min, we observe a dark circular spot, about 8 μm in radius, centred 15 μm below the needle (Fig. 1c). This spot grows in size and finally detaches from the needle (Fig. 1d). These images show the nucleation of a dislocation loop and its eventual detachment from the needle. After the first event, we observe nucleation and propagation of many more loops, which form a complex dislocation network after 600 min (Fig. 1e). Because of the complexity of this network, its three-dimensional evolution needs to be explored on the particle scale.

We use confocal microscopy to image individual particles in a 60 μm by 60 μm by 30 μm section of the colloidal crystal (Fig. 2a). This technique allows us to image the dislocations and to determine the strain field caused by the indentation. We determine individual particle positions in three dimensions with an accuracy of about 0.03 μm in the x and y directions and 0.05 μm in the z direction[12]. In this experiment, we start with the needle tip about 2 μm above the crystal surface and lower it at a rate of $2.9\,\mu m\,h^{-1}$. After 98 min, we observe a pronounced fluctuation in the crystal lattice below the needle tip, where particle rows spread apart, trying to incorporate a defect. A defect is clearly visible, as indicated by the blue arrow in the confocal microscope image of the particle configuration at $z = 15\,\mu m$ below the tip, shown in Fig. 2b. The extent of the defect is indicated by the black arrows. Remarkably, the particle rows close again after about 5 min. After five such fluctuations appear and disappear, a stable defect finally nucleates at 112 min (Fig. 2c) and grows (Fig. 2d).

To determine the full structure of the defects, we show three-dimensional reconstructions of the unstable and stable defects in Figs 2e–g. The x, y and z axes correspond to the $(1\,\bar{1}\,0)$, (110), and (001) directions of the f.c.c. lattice, respectively. At the defects, three of the six opposing nearest neighbours exhibit distorted 'bond' angles that are smaller than 180°. To visualize this, we use yellow spheres to indicate opposing particles at angles between 165° and 155°, and red spheres to indicate opposing particles at angles less than 155°. Red particles accumulate roughly 15 μm below the needle tip. They mark a surface along the hexagonal close-packed (h.c.p.) plane where the crystal has changed its stacking order, confirming that this is a planar defect. The yellow particles that lie at the boundary of this stacking fault in Fig. 2g trace the dislocation line. The Burgers vector of the dislocation is oriented along the $(1\,\bar{1}\,\bar{2})$ direction and has a length of 0.94 μm, which corresponds to the distance between adjacent wells of the h.c.p. plane. This defines the dislocation glide plane, on which defects nucleate most easily owing to the shallow potential wells. This type of dislocation is known as a Shockley partial dislocation and is the most prominent dislocation observed in f.c.c. metals. Unlike metals, where Shockley partial dislocations typically appear in pairs to reduce the extent of the stacking fault, in our

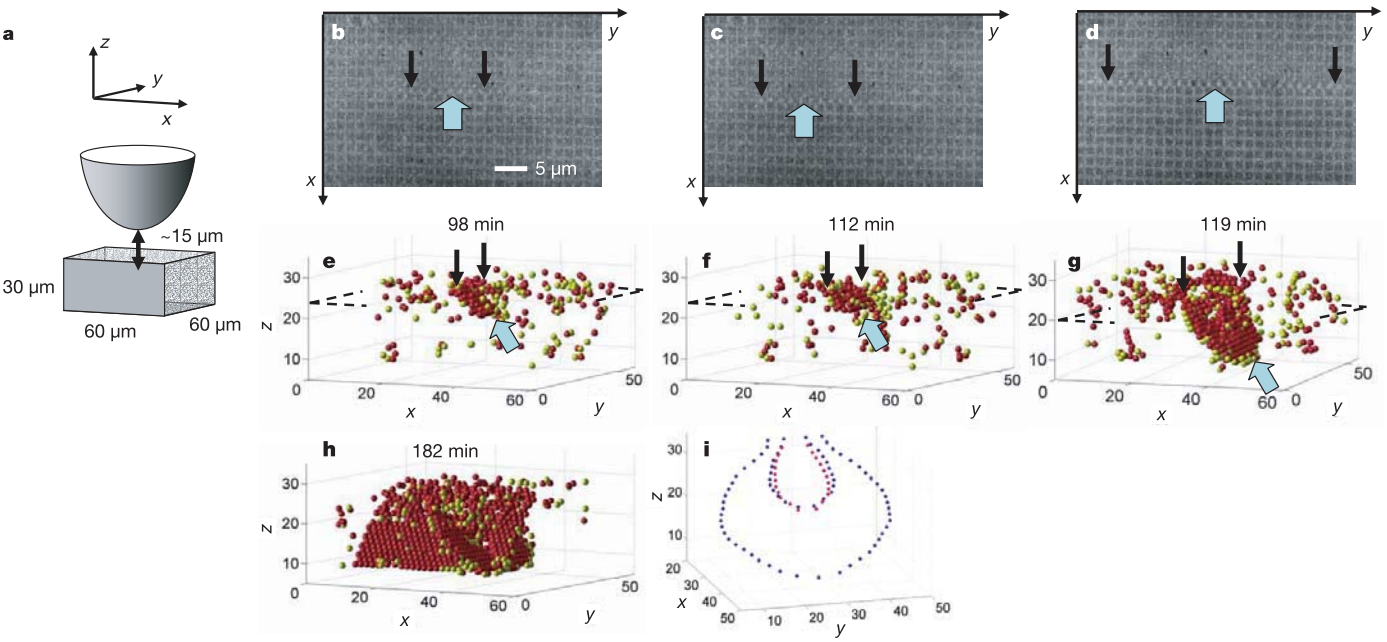

Figure 2 | Defect formation on the particle scale. **a**, Schematic showing the position of the needle tip with respect to the 60 μm by 60 μm by 30 μm crystal section depicted in **b** to **i**. **b**–**d**, Confocal microscope images of defect nucleation, taken at about 15 μm below the needle tip. **b**, Arrows indicate a defect that disappears after several minutes. **c**, Arrows indicate a defect that is stable and grows in size. **d**, Same defect as in **c** after it has fully grown. **e**–**g**, Reconstructed images of defect formation correspond to the confocal microscope images **b**–**d**. Yellow and red spheres indicate particles with slightly and highly distorted nearest-neighbour configurations, respectively. Arrows indicate stacking faults that are bound by a Shockley partial dislocation. Dashed lines at $z \approx 20\,\mu m$ indicate the height at which the confocal images are taken. **h**, Reconstruction shows a second stable defect, which nucleates on an adjacent intersecting plane. This defect appears at $t = 154$ min. **i**, Traces of the dislocation lines that surround the defects depicted in **e**–**g**. The red dots trace the dislocation line that surrounds the defect in **e**. The blue dots trace the dislocation lines that surround the stable defect shown in **f** and **g**. These traces were determined from the raw confocal images such as those in **b**–**d** by pinpointing the intersection of the dislocation line (black arrows in **b**–**d**) with the image planes.

colloidal crystal these dislocations appear to be unpaired. This difference results from the vanishingly low energy cost associated with stacking faults in hard-sphere crystals. A second dislocation is nucleated on an adjacent intersecting plane at $t = 182$ min, as shown in Fig. 2h.

These microscopic observations provide a unique opportunity for direct measurement of the critical radius, r_c. We trace the dislocation lines that surround the defects shown in Figs 2e–g by carefully examining the confocal images (Fig. 2i legend). The traces reveal circular loop shapes that open towards the crystal surface (Fig. 2i). The radius of the unstable defect (Fig. 2i, red dots) is approximately 5 μm while the radius of the stable defect (Fig. 2i, blue dots, small loop) is 7 μm; thus, $r_c \approx 6$ μm.

To explore the mechanism that drives the nucleation of these defects, we determine the components of the applied strain along the h.c.p. planes, where the defects nucleate. The elastic strain tensor is determined from the distortion in the configurations of the nearest neighbours of the particles. For each particle, we compare the vectors $\mathbf{d}_i$ to its 12 nearest neighbours i with the nearest-neighbour vectors $\mathbf{D}_i$ of the ideal f.c.c. lattice. The best affine deformation tensor, α, that transforms the ideal vectors, $\mathbf{D}_i$, to the real vectors, $\mathbf{d}_i$, is determined by minimizing the mean square difference $\sum_i(\mathbf{d}_i - \alpha\mathbf{D}_i)^2$ (ref. 13). The symmetric part of α corresponds to the local strain tensor of the particle under consideration. To smooth the resulting strain distribution, we average the strain tensor for each particle with those of its nearest neighbours and assign the resultant average strain tensor, ε_{ij}, to the particle under consideration.

The advantage of using confocal microscopy to image individual particles and measure the full strain tensor is that we can determine γ, the shear component of the strain on the $(1\ \bar{1}\ 1)$ plane where the first defect nucleates. To implement this new method of determining the shear strain, we calculate the average strain tensor ε'_{ij} in a rotated coordinate system, in which the x' and z' axes align with the $(1\ \bar{1}\ \bar{2})$ and $(1\ \bar{1}\ 1)$ directions, respectively. We take $\gamma = 2\varepsilon'_{x'z'}$. We illustrate various cuts through the crystal, and represent the magnitude of γ with colour. The γ distribution shortly before the defect in Fig. 2e nucleates is shown in Fig. 3a and b. A region of high positive shear strain (red) is centred approximately 10 μm below the needle, where the average value of γ is approximately 0.06. Strikingly, the shape of this strain distribution matches the contrast profile observed with LDM (Fig. 1b). Defect nucleation occurs entirely in this region of high shear strain.

The strain field changes drastically after the first dislocation nucleates. To highlight this change, in Fig. 3c we plot the γ distribution along the y–z plane that intersects the dislocation loop along its diameter and is perpendicular to the cut shown in Fig. 3a. The negative shear strain induced by the dislocation loop (blue) reduces the cumulative strain that drives nucleation of a second dislocation on the same glide plane. In contrast, the distribution of γ', the component of the strain on the (111) plane, still has a region of high positive strain (Fig. 3d). This results in the nucleation of a second dislocation loop in an adjacent, but intersecting h.c.p. plane (Fig. 2h).

The distribution of γ in Fig. 3c shows that the negative shear strain regions (blue) inside the dislocation loop almost overlap. Because the contrast in the LDM images arises from these lattice distortions, this observation validates our interpretation that small dislocation loops appear as dark spots in Fig. 1c and d. This strain distribution also allows us to determine the precise position of the dislocation loop and where it intersects the y–z plane in Fig. 3c. To accomplish this, we focus on particles within 1.6 μm of the dashed line and plot γ versus y in Fig. 3e. The strain diverges on both sides of the dislocation with the divergence truncated at the dislocation core. The crossovers at $y = 7$ and $y = 45$, where γ switches sign, demarcate precisely the intersection of the dislocation with the y–z plane. This is in excellent agreement with the location of the dislocation line shown in Fig. 2i.

The precision of our measurements presents an opportunity to make direct comparisons with continuum models[14–16]. We consider

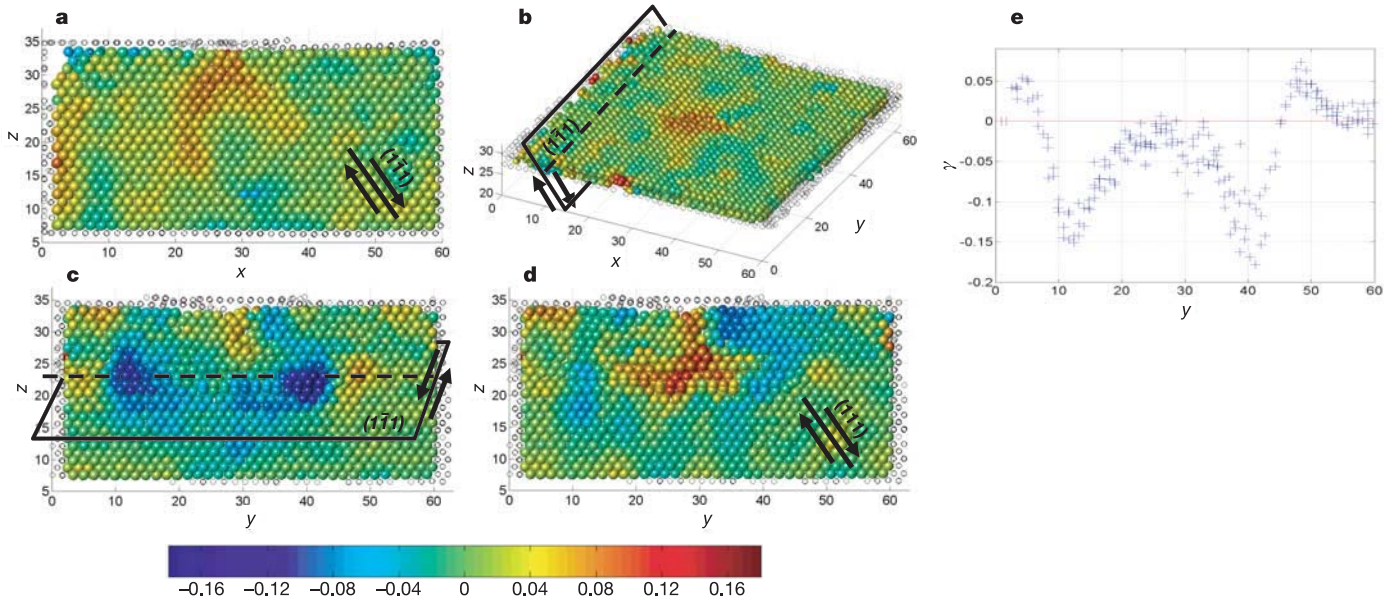

Figure 3 | Strain distribution in the indented crystalline film. Particle colour in **a**–**d** indicates the value of the local shear strain (see colour scale). Positive shear strain is indicated by arrows in each figure. **a**, **b**, Two cuts showing the distribution of γ, the shear strain component on the $(1\ \bar{1}\ 1)$ plane along $[1\ \bar{1}\ \bar{2}]$ at $t = 91$ min. **a**, 3-μm-thick x–z crystal section centred below the needle at $y = 29$ μm. **b**, 3-μm-thick x–y crystal section located 10 μm below the needle at $z = 29$ μm. **c**, **d**, Two cuts showing the strain distribution at $t = 119$ min, shortly after the first dislocation loop nucleated. Both figures show a 3-μm-thick y–z section at $x = 33$ μm, which intersects the loop at a diametrical plane. **c**, Distribution of γ, the component of the shear strain on the defect plane. Adjacent regions of high negative shear strain (blue particles) and moderately positive shear strain (yellow particles) are observed. **d**, Distribution of γ', the shear strain component on the intersecting {111} plane. In contrast to **c**, a central region of high positive shear strain is observed below the needle tip. **e**, Shear strain values versus y for particles within 1.6 μm of the dashed line at $z = 23$ μm in **c**. γ switches sign at $y = 7$ μm and $y = 45$ μm. This demarcates where the dislocation line intersects the y–z plane.

the crystal to be an isotropic, linear elastic medium with Young's modulus E, shear modulus μ, and Poisson ratio ν. The high shear strain region of the elastically deformed lattice (Fig. 3a) is observed at roughly 0.8 times the contact radius below the needle tip. The location of the shear strain maximum is in good agreement with hertzian theory for the strain distribution under an indenting tip[17]. It is also in good agreement with measurements of a two-dimensional model system formed from bubble rafts[6]. Experiments with needles of different size showed a shift of the shear strain maximum in accordance with the predictions of hertzian theory.

The role of thermal fluctuations can also be quantitatively addressed. The energy cost to create a dislocation loop of radius r is $A(\mu b^2 r/2)\ \ln(r/r_0)$, where r_0 is the effective core radius of the dislocation strain field, b is the length of the Burgers vector, and A is a constant that accounts for the mixed edge–screw topology of a dislocation loop[14–16]. The energy gain from relief of the overall strain is $\pi r^2 b\tau$, where τ is the local stress before dislocation nucleation. The total nucleation energy has a maximum at $r_c = (A/4\pi)\gamma b\ \ln(r_c/r_0)$, while the critical energy at $r = r_c$ is $U_c = A(\mu b^2 r_c/4)\ln(r_c/r_0)$. Here, we have used $\gamma = \tau/\mu$. We calculate A by averaging over the edge and screw components of the dislocation loop to yield $A = 5/4$ (ref. 15). In addition, we include the additional energy stored within the dislocation core and use $r = b\exp(-0.4) = 0.67b$ (ref. 15). We plot the resultant r_c/b and $U_c/\mu b^3$ versus γ in Figs 4a and b. Both r_c and U_c decrease monotonically with increasing γ. The theoretical shear strength corresponds to the value of the stress at $U_c = 0$. Beyond this stress, dislocations form even in the absence of thermal fluctuations and this description breaks down. The vertical dashed line and shaded bar centred at $\gamma = 0.06$ correspond to the mean of γ and the standard deviation of the mean in the high strain region. The shaded horizontal bar centred at 6.4 marks the possible range for r_c/b determined from the experiment. The intersection of the shaded regions is close to the calculated curve, which confirms that this continuum model can be applied to our system.

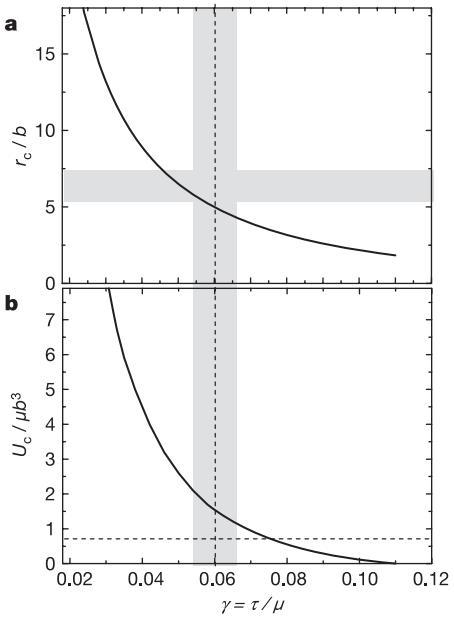

Figure 4 | Continuum model prediction for the critical radius and energy of dislocation nucleation. a, Dimensionless critical radius r_c/b versus shear strain for $r_0 = 0.67b$. The grey horizontal bar indicates the range of r_c/b values determined from experiments. The dashed vertical line and shaded bar centred at $\gamma = 0.06$ indicate the mean of γ and the standard deviation of the mean in the high shear strain region under the indenter. **b**, Critical nucleation energy versus shear strain. The dashed horizontal line at $U_c/\mu b^3 = 0.7$ indicates the value for the critical energy determined from experiments.

Further confirmation of the model comes from comparison of the measured and predicted values for U_c. We determine U_c from the observed nucleation rate using $J = f_0\ m\exp(-U_c/kT)$, where m is the total number of particles in the high stress region and f_0 is a characteristic frequency of the particles. We estimate the nucleation rate from the time between fluctuations, $2 \times 10^{-3}\ \mathrm{s}^{-1}$. We estimate f_0 from the timescale τ required for a particle to diffuse in its local well until it reaches its nearest neighbour. The distance a particle moves is $\delta \approx 0.08\ \mu\mathrm{m}$. Because $\tau = (\pi\eta a\delta^2/kT)$ (ref. 18), where a is the particle radius, k is Boltzmann's constant, T is the temperature and the solvent viscosity is $\eta = 3 \times 10^{-3}$ Pa s (ref. 19), we find $\tau \approx 10^{-2}$ s yielding a frequency of $f_0 = 100\ \mathrm{s}^{-1}$. Furthermore, we estimate $m = 125$ from the observation that the high shear strain region extends about five particle diameters in the x, y and z direction. Thus, we obtain $U_c/kT = 16$, which yields a critical nucleation energy of about 0.41 eV. Finally, using $\mu = E/[2(1+\nu)]$ with $\nu = 1/3$ (ref. 20), $E = 0.3$ Pa (ref. 2), and $b = 0.94\ \mu\mathrm{m}$, we obtain $U_c/\mu b^3 = 0.7$, which is marked by the horizontal dashed line in Fig. 4b. The model predicts a value that is a factor of two larger than our estimate, which is well within the uncertainty of our estimate of $U_c/\mu b^3$.

Nano-indentation experiments on atomic systems typically entail measurements of force–displacement relationships[3–5]. Values of forces required for indentations of atomic systems are typically several tens of micronewtons. By comparison, from the measured strain, the elastic modulus, and the contact area of the indenter, we estimate that the forces required to induce defects in these colloidal crystals are only several piconewtons and cannot be measured. We can determine the origin of this difference by estimating the shear modulus to be $\mu = U_b/a^3$, where U_b is the interaction energy. Then the difference between these forces reflects the number of particles under the tip, which leads to a factor of $\sim$400, the bond energies, which lead to a factor of $\sim$50, and the size of the particles, which leads to a factor of $\sim 10^4$; the net result gives a difference of 2×10^8, in reasonable agreement with our estimate.

The advantage of investigating colloidal systems, however, is that we can directly image the microscopic strain field, which allows us to follow the thermal activation of dislocation loops precisely and to measure the critical size for their nucleation. The value of $U_c = 16kT$ reflects the diverging entropic cost for changing particle configurations near the close-packed limit of the colloidal crystal. By comparison, in atomic systems at equal nucleation rates, the value of U_c is a factor of two higher, reflecting that the attempt frequency is ten orders of magnitude higher. Values of μb^3 for a compliant metal such as aluminium are also only a factor of two higher than estimates for μb^3 in our colloidal suspension. Remarkably, the ratio $U_c/\mu b^3$ (Fig. 4b) is unchanged, which indicates that the effects of thermal fluctuations in our experiment are similar to those in a typical nano-indentation experiment; they should therefore be observed in experiments that have sufficiently accurate strain control.

Received 12 May; accepted 19 December 2005.

1. Hirth, J. P. & Lothe, J. *Theory of Dislocations* Edn 2 (Wiley, New York, 1982).
2. Schall, P., Cohen, I., Weitz, D. A. & Spaepen, F. Visualization of dislocation dynamics in collidal crystals. *Science* **305**, 1944–1948 (2004).
3. Suresh, S., Nieh, T.-G. & Choi, B. W. Nano-indentation of copper thin films on silicon substrates. *Scr. Mater.* **41**, 951–957 (1999).
4. Kiely, J. D., Jarausch, K. F., Houston, J. E. & Russell, P. E. Initial stages of yield in nanoindentation. *J. Mater. Res.* **14**, 2219–2227 (1999).
5. Li, J., van Vliet, K. J., Zhu, T., Yip, S. & Suresh, S. Atomistic mechanism governing elastic limit and incipient plasticity in crystals. *Nature* **418**, 307–310 (2002).
6. Gouldstone, A., Van Vliet, K. J. & Suresh, S. Simulation of defect nucleation in a crystal. *Nature* **411**, 656 (2001).
7. Kelchner, C. L., Plimpton, S. J. & Hamilton, J. C. Dislocation nucleation and defect structure during surface indentation. *Phys. Rev. B* **58**, 11085–11088 (1998).
8. Lilleodden, E. T., Zimmerman, J. A., Foiles, S. M. & Nix, W. D. Atomistic simulations of elastic deformation and dislocation nucleation during nanoindentation. *J. Mech. Phys. Sol.* **51**, 901–920 (2003).

9. Stach, E. A. *et al.* Development of a nanoindenter for in situ transmission electron micoroscopy. *Microsc. Microanal.* **7,** 507–517 (2001).
10. Minor, A. M., Lilleodden, E. T., Stach, E. A. & Morris, J. W. Direct observation of incipient plasticity during nanoindentation of Al. *J. Mater. Res.* **19,** 176–182 (2004).
11. van Blaaderen, A., Ruel, R. & Wiltzius, P. Template-directed colloidal crystallization. *Nature* **385,** 321–324 (1997).
12. Weeks, E. R., Crocker, J. C., Levitt, A. C., Schofield, A. & Weitz, D. A. Three-dimensional direct space imaging of structural relaxation near the colloidal glass transition. *Science* **287,** 627–631 (2000).
13. Falk, M. L. & Langer, J. S. Dynamics of viscoplastic deformation in amorphous solids. *Phys. Rev. E* **57,** 7192–7205 (1998).
14. Frank, F. C. in *Symposium on Plastic Deformation of Crystalline Solids* 89–102 (Carnegie Institute of Technology and Office of Naval Research, Pittsburgh, 1950).
15. Hirth, J. P. in *The Relation Between the Structure and the Mechanical Properties of Metals* 217–228 (Her Majesty's Stationery Office, London, 1963).
16. Cottrell, A. H. *Dislocations and Plastic Flow in Crystals* (Oxford Univ. Press, Oxford, 1956).
17. Davies, R. M. The determination of static and dynamic yield stresses using a steel ball. *Proc. R. Soc. Lond. A* **197,** 416–432 (1949).
18. Chaikin, P. M. & Lubensky, T. C. *Principles of Condensed Matter Physics* Ch. 7.4.5 (Cambridge Univ. Press, Cambridge, 1995).
19. Higashigaki, Y., Christensen, D. H. & Wang, C. H. Studies of the reorientational motion and intermolecular interaction of dimethylsulfoxide in water by depolarized Rayleigh-scattering. *J. Phys. Chem.* **85,** 2531–2535 (1981).
20. Frenkel, D. & Ladd, A. J. C. Elastic constants of hard-sphere crystals. *Phys. Rev. Lett.* **59,** 1169 (1987).

Supplementary Information is linked to the online version of the paper at www.nature.com/nature.

Acknowledgements We thank R. Christianson and D. Blair for their help with the image analysis, M.L. Falk for discussions about the strain algorithm, and D. Bonner for help with programming the strain algorithm. This work was supported by a Lynen Fellowship from the Alexander von Humboldt Foundation (P.S.), and by NSF and Harvard MRSEC grants.

Author Information Reprints and permissions information is available at npg.nature.com/reprintsandpermissions. The authors declare no competing financial interests. Correspondence and requests for materials should be addressed to P.S. (pschall@science.uva.nl).